AD-A172 713 MICROWAVE ACOUSTICS DEVICE STUDY(U) IOWA STATE UNIV 1/1
AMES K M LAKIN 22 JUL 86 AFOSR-TR-86-0860
AFOSR-84-0386

UNCLASSIFIED F/G 9/1 NL

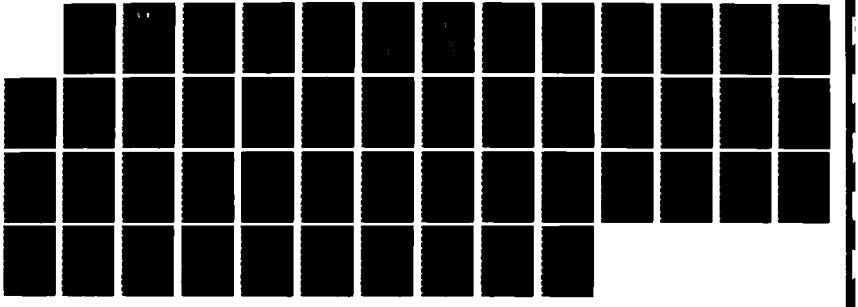

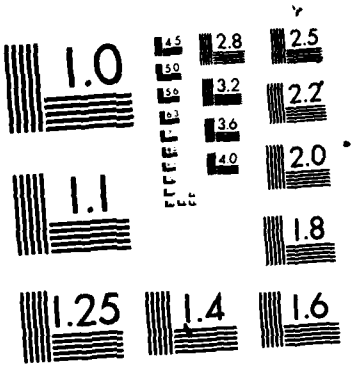

(2)

Unc

SECURITY

AD-A172 713

DOCUMENTATION PAGE

DTIC ELECTE OCT 0 8 1986 S D

1a. REPORT SECURITY CLASSIFICATION: Unclassified	1b. RESTRICTIVE MARKINGS: N/A
2a. SECURITY CLASSIFICATION AUTHORITY: N/A	3. DISTRIBUTION/AVAILABILITY OF REPORT: Unlimited
2b. DECLASSIFICATION/DOWNGRADING SCHEDULE: N/A	
4. PERFORMING ORGANIZATION REPORT NUMBER(S): N/A	5. MONITORING ORGANIZATION REPORT NUMBER(S): AFOSR-TR- 86-0980
6a. NAME OF PERFORMING ORGANIZATION: Iowa State University; 6b. OFFICE SYMBOL (If applicable):	7a. NAME OF MONITORING ORGANIZATION: Air Force Office of Scientific Research
6c. ADDRESS (City, State and ZIP Code): Ames, Iowa 50011	7b. ADDRESS (City, State and ZIP Code): Building 410, Bolling AFB, DC 20332-6448
8a. NAME OF FUNDING/SPONSORING ORGANIZATION: Air Force Office of Scientific Research; 8b. OFFICE SYMBOL (If applicable): AFOSR	9. PROCUREMENT INSTRUMENT IDENTIFICATION NUMBER: AFOSR 84-0386
8c. ADDRESS (City, State and ZIP Code): Building 410, Bolling AFB, DC 20332=6448	10. SOURCE OF FUNDING NOS. — PROGRAM ELEMENT NO.: 61102F; PROJECT NO.: 2306; TASK NO.: B2; WORK UNIT NO.:
11. TITLE (Include Security Classification): Unclassified — Microwave Acoustics Device Study	
12. PERSONAL AUTHOR(S): K.M. Lakin	
13a. TYPE OF REPORT: Final; 13b. TIME COVERED: FROM 84-9-1 TO 85-8-31; 14. DATE OF REPORT (Yr., Mo., Day): 86-7-22; 15. PAGE COUNT: 47	
16. SUPPLEMENTARY NOTATION: N/A	

17. COSATI CODES			18. SUBJECT TERMS (Continue on reverse if necessary and identify by block number)
FIELD	GROUP	SUB. GR.	microwave acoustics, thin film resonators, bulk acoustic waves, diffusion of Zn, GaAs

19. ABSTRACT (Continue on reverse if necessary and identify by block number)

This final report summarizes the results of a single one year study of the device physics aspects of the thin film bulk acoustic wave resonator. The study involved high Q trapped energy resonators, zinc diffusions in GaAs as a precursor to temperature coefficient studies, and refinements to the two dimensional numerical analysis modeling of microwave acoustic boundary value problems by the finite difference method.

20. DISTRIBUTION/AVAILABILITY OF ABSTRACT: UNCLASSIFIED/UNLIMITED ☒ SAME AS RPT. ☐ DTIC USERS ☐	21. ABSTRACT SECURITY CLASSIFICATION: Unclassified
22a. NAME OF RESPONSIBLE INDIVIDUAL: Capt. Kevin Malloy	22b. TELEPHONE NUMBER (Include Area Code): (202) 767-4931; 22c. OFFICE SYMBOL: AFOSR AFSC/NE

DD FORM 1473, 83 APR — EDITION OF 1 JAN 73 IS OBSOLETE. — UNCLASSIFIED

SECURITY CLASSIFICATION OF THIS PAGE

AFOSR-TR- 86-0840

Table of Contents

1.0 INTRODUCTION

The following report summarizes the work done on a one year research project on microwave acoustic devices, principally topics related to the thin film resonator, TFR.

Prior and concurrent work supported by AFOSR was on thin film materials of ZnO, AlN, and $LiNbO_3$ deposited by the sputtering process. These films were evaluated in the TFR device configuration. In the course of the materials program, it became apparent that the TFR is a potentially valuable device per se whose device physics problems need further study.

Device physics problems of the TFR that required further study are the multidimensional boundary value problem of microwave acoustic modal analysis, temperature and aging effects, and limits of TFR performance in the 1-2 GHz frequency range.

Because of the limited duration of this project (one year), the topics had to be limited to the personnel and prior experience resources available. In particular the two dimensional numerical analysis of the TFR had been formulated but needed further refinement. A prior project from RADC that had initiated a study of doping effects on acoustical properties in GaAs was followed here by a study of deep Zn diffusions. Finally, a study of acoustical mode trapping effects was initiated in order to determine the lower limits of resonator Q in the 1-2 GHz frequency range. Because of the limited duration of funding only MSEE degree level efforts could be supported.

The next three sections is a summary of the projects and progress made during the one year of funding.

2.0 HIGH Q RESONATORS

2.1 Introduction

Resonator Q is an important parameter that characterizes resonator performance in oscillator and filter circuits. The resonator Q is related to the quality of the material and topology of the films.

The thin film resonator is a material composite in the configurations shown in Figs 2.1 and 2.2. Research efforts were directed toward improving the Q of the Si base resonators by adjusting sputtering conditions to improve film quality and electrode design in the configuration of Fig 2.1.

2.1.1 Film Substrate Evaluation

The most definitive piezoelectric film evaluation is the measurement of the film's piezoelectric coupling coefficient and Q.

Measurements of unloaded Q are inferred from the resonator impedance as derived from transmission line reflection coefficient data measured on an HP 8510T network analyzer. The resonator Q is calculated from the measured impedance data using the relation

$$Q = \frac{fr}{2} \frac{dZ\phi}{df}\bigg|_{fr}$$

where $Z\phi$ is the phase of the impedance and fr is the resonant frequency defined implicitly as the frequency of maximum Q.

The electromechanical coupling coefficient K^2 of a resonator is also an important quantity for filter synthesis applications because it affects the filter performance in two ways. First, the pole-zero separation is dependent upon K^2 with larger K^2 being capable of synthesizing wider bandwidths. Second, the resonant series resistance is scaled by K^2 and the

THIN FILM RESONATORS

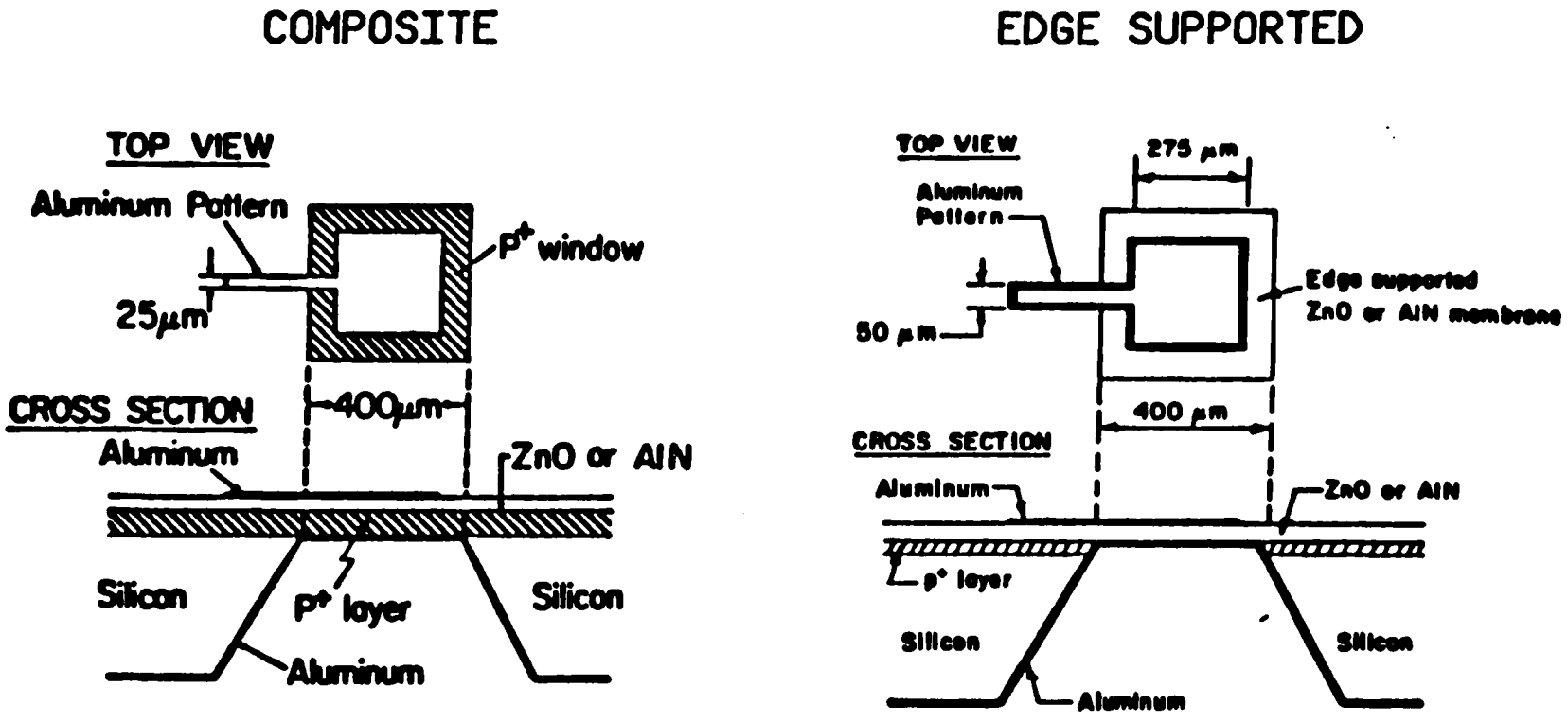

Fig. 2.1 Side view of thin film resonators formed on Si substrates. Thick (<10μm) P^+ membrane is formed by top-side wafer diffusion followed by bottom-side chemical etch. Sputter deposition of ZnO or AlN or other piezoelectric film forms the excitation region. Metal films form the electrodes. The generated sound wave bounces between the two surfaces and at certain frequencies adds in phase to give a resonance. a) a composite structure, b) an edge supported film formed by reactive ion etching the P^+ layer.

RESONATORS ON GaAs BY TOP-SIDE PROCESSING

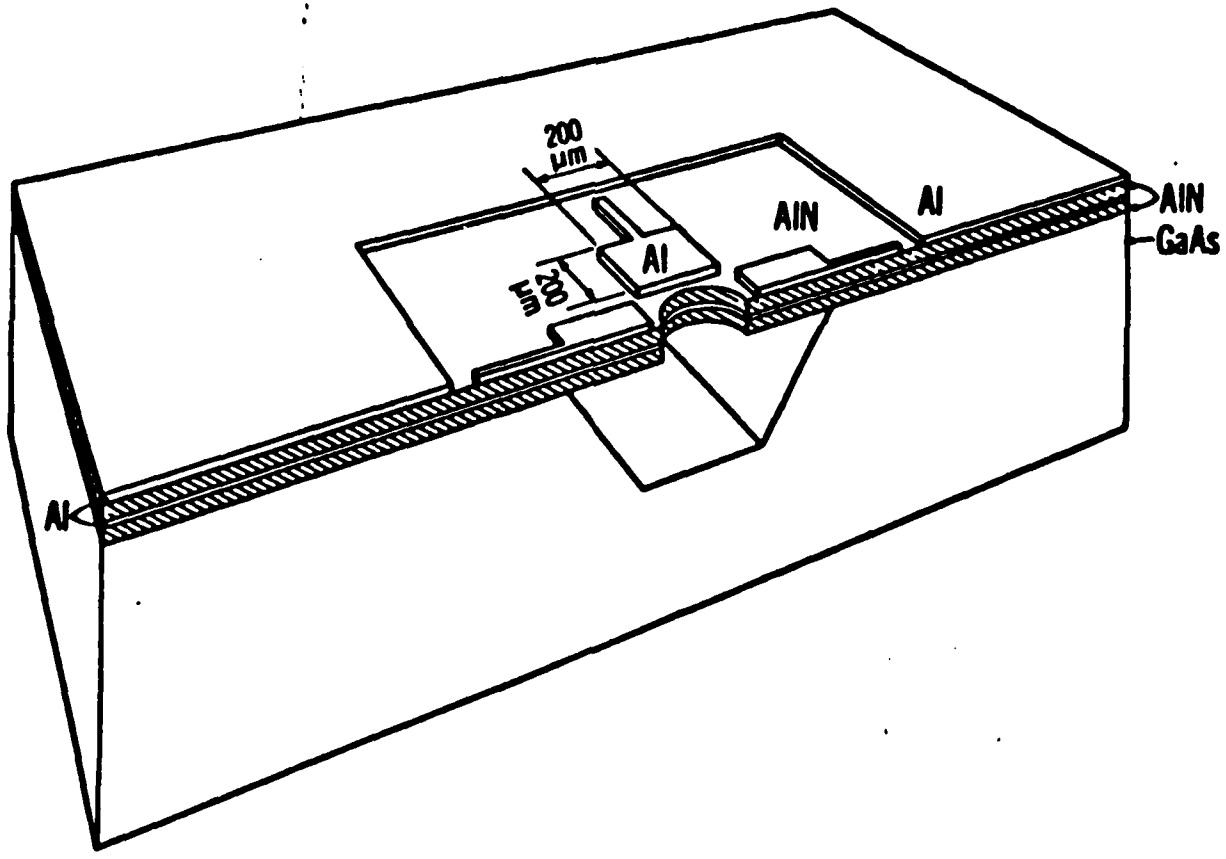

Fig. 2.2 Resonator formation on GaAs. The composite is formed by a sequence of piezoelectric AlN and Al metal depositions. Next, a small hole is etched in the composite to expose the GaAs substrate. Chemical GaAs etch then undercuts the membrane to form an edge supported structure. More than one resonator can be fabricated on a single membrane, as shown.

capacitive reactance of the structure. For a one dimensional resonator which has a very large diameter to thickness ratio, the coupling coefficient is determined from

$$K^2 = \phi_r/\tan\phi_r$$

where

$$\phi_r = \frac{\pi}{2} fs/fp$$

fs = series resonant frequency

fp = parallel resonant frequency

The K^2 determined from this relation for nonideal resonators is referred to as an effective K^2 since the value is not simply related to fundamental material parameters.

The best method of measuring these macroscopic film properties is to use a resonator in one of the accepted configurations. In all such cases the measurement is subject to artifacts due to the measuring structure. These macroscopic factors are discussed below.

Energy Trapping. The degree of energy trapping is a function of the device geometry and specific resonant mode. Resonator Q is a function of energy trapping and measurements indicate a minimum material Q for a specific mode. Thus, a resonator structure that allows transverse acoustic radiation along the membrane and into the substrate would exhibit a lower Q.

Electrode Metallization Effect. Resonator acoustic losses are increased by the relatively high acoustical loss in metals compared to the piezoelectric. Thinner metal electrodes reduce mechanical losses but increase the electrical resistance. Note that increased metal thickness immediately

within to the resonator will cause the wave to migrate to the thicker or slower structure and hence lead to trapping. The electrode resistance effect is most pronounced at series resonance where large displacement currents in the piezoelectric must flow through the electrode metal. This affect is observed as a lower series resonant Q as compared to parallel resonance Q.

Geometrical Defects. Surface contamination reduces resonator Q and causes frequency shifts. Etching imperfections such as Pits or hillocks give false resonator operation due to mode shifts and scattering losses.

Stray Capacitance. Stray capacitance in the electrodes appear in parallel with resonator and causes the parallel resonant frequency to decrease. The reduced pole-zero spacing reduces the apparent coupling coefficient and lowers the achievable filter bandwidth.

Interpretation of Q and K^2 measurements must be done with some caution. The K^2 as defined by the phase slope definition of series and parallel resonance may depart from the material K^2 for low Q resonators. Consequently, a change in material growth conditions or resonator geometry that appears to have increased K^2 may in reality have reduced Q and the resultant spread in phase incorrectly interpreted as increased material K^2.

In order to evaluate films with the least ambiguity we have adopted the following procedures:

1. Films not in resonator configurations or deposited over the whole wafer are optically examined by Normarski microscopy, x-ray diffraction, and when appropriate Auger chemical analysis (to determine oxygen in AlN to 0.1% levels) or electron microscopy.

2. Resonator film structures are first examined by Normarski phase contrast microscopy to find structural defects and subsequent electrical evaluation is done by one-port microwave reflection measurements. From the electrical data, series metallization resistance, series and parallel resonant frequencies and respective Qs, and finally, the uncorrected piezoelectric coupling coefficient are obtained.

2.1.2 Resonator Analysis and Modeling

Resonator analysis and modeling takes two basic forms. These are the one-dimensional models used for ideal resonators and the approximate lumped element circuit models (Butterworth Van Dyke) used for some synthesis applications. Only the one dimensional Mason model (Fig. 2.3) can be derived from first principles. A two dimensional numerical analysis based model is described in section 3.0.

The one dimensional Mason model is extremely useful because it can be used to model the performance of a single mode, and with modification, multimode two and three dimensional resonators. Basically, the Mason bulk wave model treats the piezoelectric plate as a three port network having one electrical port and two acoustical ports.

2.2 Experimental Results

The measured results shown in Fig. 2.4 were for an AlN/p^+Si membrane resonator fabricated by selective etching of the Si membrane followed by dc planar magnetron deposition of the AlN. Series resonance Q was approximately 1500 and parallel resonance Q was 5000. The decreased series Q was found to be due to a finite (one ohm per square) sheet resistance in the metal electrode.

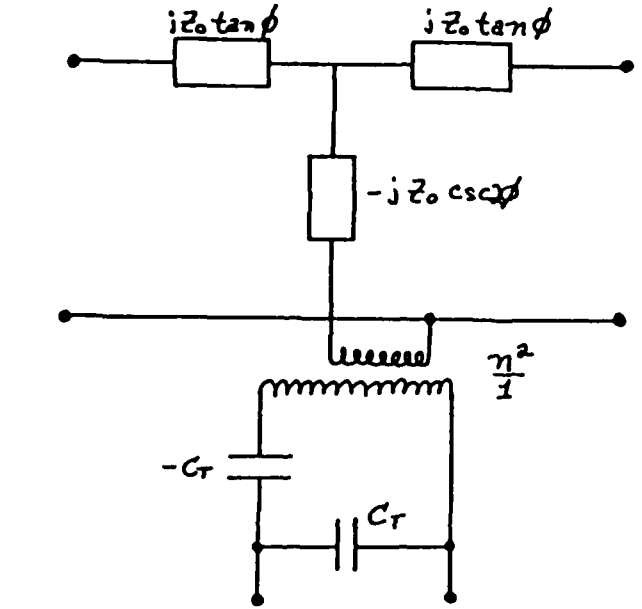

$n^2 = \frac{K^2}{2\phi}\omega C_T Z_o$ $\quad C_T$ = capacitance

K^2 = Coupling Coefficient $\quad Z_o$ = mechanical Impedance

2ϕ = acoustic phase

a)

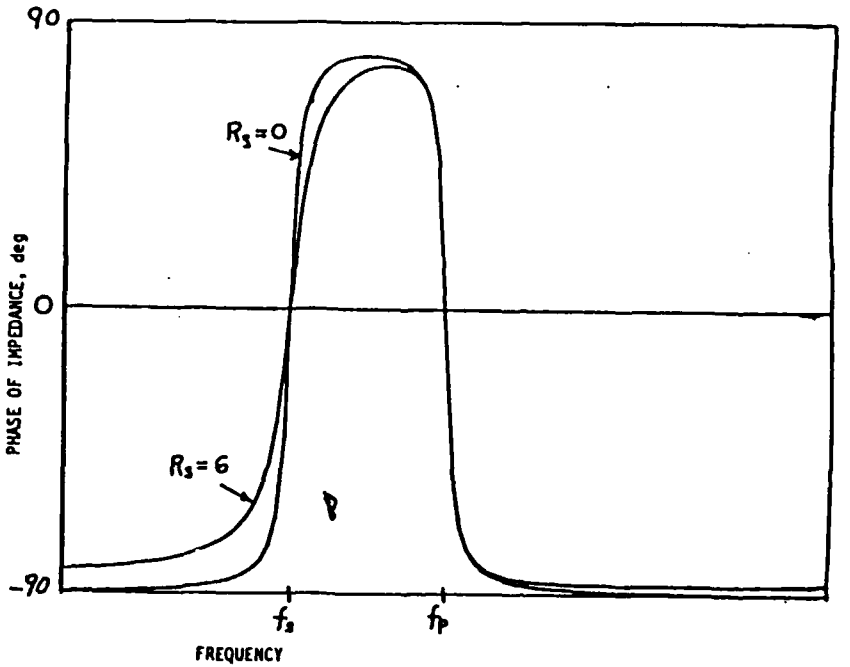

b)

Figure 2.3 Examples of resonator modeling. a) Mason lumped element equivalent model for a one-dimensional or single mode resonator. This model is used for crystal filter analysis and response predictions of an ideal resonator. b) Example calculation of the phase of the resonator impedance, and hence Q_l as a function of frequency. Material parameters for AlN, including loss, were given the Mason model along with electrode series resistance loss. The series and parallel Q's are equal to 3,000 for Rs=0, but series Q reduces to 1,500 for Rs=6 ohms. Other effects, such as bulk wave transduction from the electrode extensions have been modeled using the Mason model.

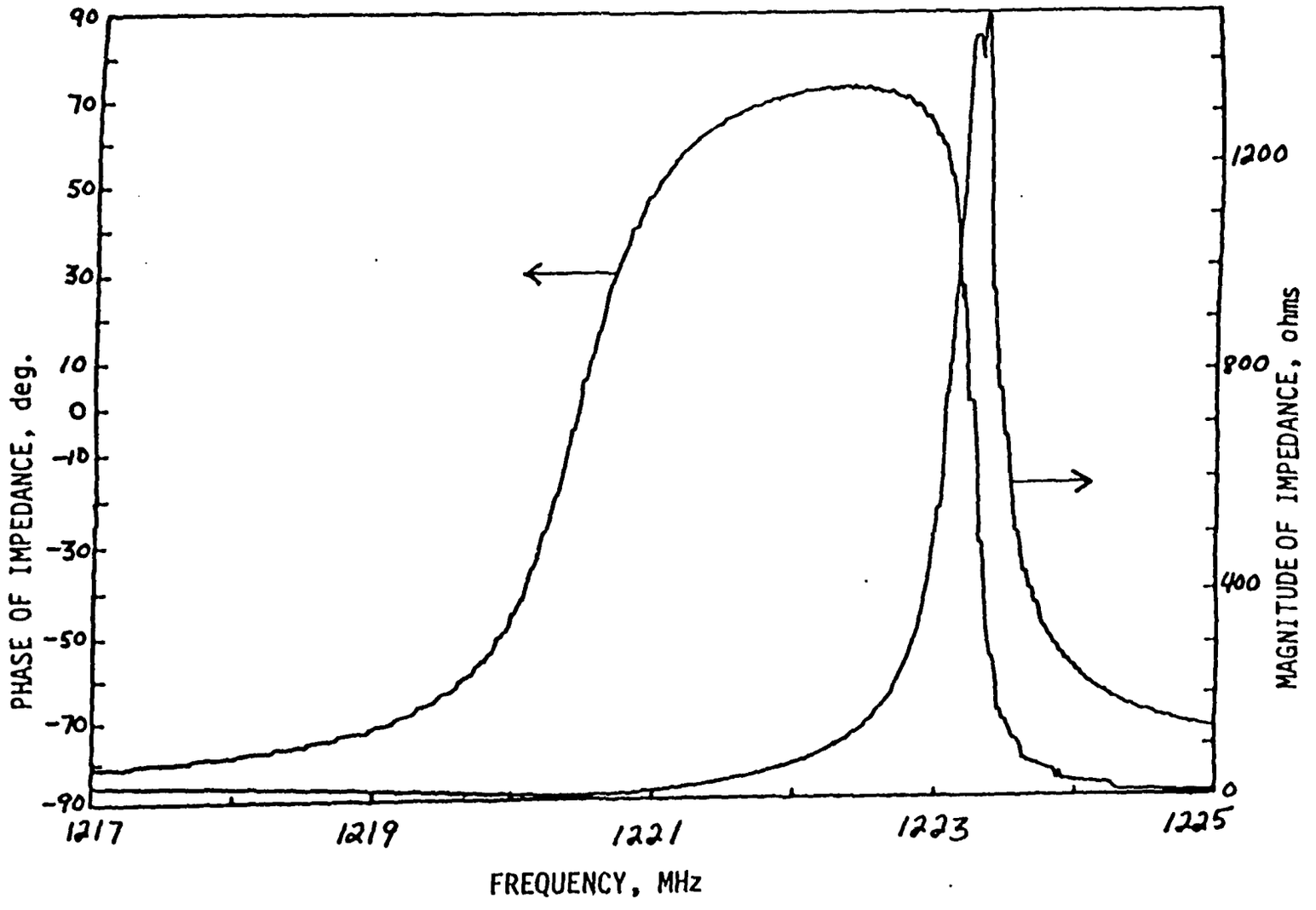

Figure 2.4 Measured response of a 1.2 GHz resonator composed of AlN on a thin Si p+ membrane. Resonance Q's were determined from phase slope measurements to be 5,000 at parallel resonance and 1,500 at series resonance. The lower series resonance was due to an added 6 ohms of resistance in the metalization trace beyond the electrode. Note first that the resonator clearly crosses the zero phase point and exhibits an extensive inductive region. Secondly, the maximum phase slop occurs near zero phase. These two features of proper resonator fabrication allow oscillator design without the need for inductor compensation of excessive shunt capacitance.

However, energy trapping was still accomplished by the electrode structure as evidenced by the high Q and multitude of anharmonic resonances. Thus the research goal of demonstrating energy trapping was accomplished.

3.0 MASKED DEEP ZINC DIFFUSIONS IN GaAS

3.1 Introduction

Temperature compensation, TC, of thin film resonators is an important feature for eventual device applications. In composite resonators TC can be accomplished by a positive-to-negative balance between two or more layers in the structure. This occurs in the composite resonators using p^+ silicon as a support structure. The experimental results [1] and theory[2] for this case are well documented.

The objective of this task was to evaluate similar effects in heavily doped GaAs structures. Previously, on an RADC project, we had evaluated purchased GaAs wafers that had been doped during growth. However, the as grown GaAs could not be doped sufficiently to achieve the high carrier concentrations necessary for the observation deformation potential coupled temperature effects and accordingly this study of diffusion in GaAs was initiated.

In order to evaluate the diffused layers, it was necessary to employ selected area diffusions and surface acoustic wave measurements. The project then became one of studying masked deep zinc diffusions in GaAs.

3.2 Results and Conclusions

The full details of the work are given in the MSEE thesis of G. Tuttle.[3] The following summary is taken from the thesis.

A capsule diffusion system for diffusing zinc into GaAs has been built and carefully characterized. The system satisfactorily forms heavily doped zinc layers in GaAs. Such deep, heavily doped layers are not possible with ion implantation. In addition, it has been shown that reactively sputtered

silicon nitride, in conjunction standard wet chemistry processing, serves as an adequate masking material to confine the zinc diffusions to selected area of a GaAs wafer. Replacement of the wet etching with plasma etching to eliminate the anomalous lateral diffusion effects observed will make silicon nitride a truly excellent masking system.

Also, using the capsule system, several attempts were made at performing n-type diffusions using tin and sulfur as the donor material. Though unsuccessful, these experiments provided some insight into what type of diffusion system might be used for performing n-type diffusion in GaAs.

The question naturally arises as to what value the zinc diffusions are without the n-type diffusions needed for fabricating high performance GaAs transistors. Perhaps the most obvious use is in making p^+ contacts to electronic devices having p-layers as part of their structure. In addition, other semiconductor devices such as lasers, LEDs, and GaAs solar cells need diffused layers and ohmic contacts.

If GaAs substrates are available with an n-type doping of 10^{-16} cm^{-3} or less, the zinc diffusions and silicon nitride masking can immediately be applied towards making a self-aligned metal insulator semiconductor field effect transistor (MISFET). All that is needed is to diffuse the source and drain regions through a SiN_x mask, deposit and pattern the gate, source, and drain metal concurrently, and an enhancement-mode p-channel MISFET is finished in two simple steps. The SiN_x between the source and drain serves double duty as a diffusion mask and gate dielectric. Albeit, this is a low frequency device, but it would still have application as a biasing element or active load in a high frequency digital or microwave circuit.

The zinc diffusions and SiN_x masking could also be used in conjunction with ion implanted n-type layers as the diffused gate of a JFET. The JFET should have certain advantages over the MESFET. The JFET should be a higher

frequency device, with diffusion the pinch-off voltages should be more reproducible from device to device and wafer to wafer, and the JFET should be able to tolerate larger voltage swings at the gate.

Also, using the Gaussian type diffusions that were demonstrated, p-channel MESFETs and JFETs (if used with an n-type implanted gate) should be possible. However, more work is required in characterizing these Gaussian diffusions.

One last application is related to the acoustic properties of GaAs. It has been shown both theoretically and experimentally that the temperature dependence of the elastic constants of silicon changes when the silicon is heavily doped with boron. This can be used to form signal processing devices that do not change characteristics as the temperature changes. It would be very desirable to do this with GaAs. In ongoing experiments, the temperature dependence of both doped and undoped GaAs is being measured using surface acoustic waves traveling in undoped and heavily zinc-doped GaAs. If GaAs shows the same change in temperature dependence that silicon does, temperature compensated acoustic devices on GaAs will become possible.

---

1. F.S. Kahn and P.B. Allen, "Temperature Dependence of the Elastic Constants of p^+ Silicon," Phys. Stat. Sol.(b) 128, 31 (1985).

2. J.S. Wang and K.M. Lakin, "Low-Temperature Coefficient Bulk Acoustic Wave Composite Resonators," Appl. Phys. Lett. 40(4), 15 Feb. 1982.

3. G. Tuttle, "A Technique for Silicon Nitride and Aluminum Nitride Masked Deep Zinc Diffusions in Gallium Arsenide," Iowa State University, 1985.

4.0 FINITE DIFFERENCE CALCULATIONS

4.1 Introduction

In order to treat a general class of piezoelectric excitation problems, a finite difference formulation has been developed to study the two dimensional coupled piezoelectric wave equation [3]. The formulation allows for three displacement components and an electric potential, complicated boundary configurations, and arbitrary material anisotropy. This study will test the formulation on a specific resonator structure.

Some simple geometrical structures have been analyzed by others using different methods such as plate wave mode expansions. These methods however, assume infinite dimensions in some particular directions and/or have restricted boundary conditions [6,7,9,10, and 12]. They can not account for changes in material thickness and require material uniformity throughout the region.

4.2 Development of the Numerical Method

The theoretical development of the finite difference formalism starts from the general point form linear elastic equations for arbitrary anisotropy,

$$\frac{\partial}{\partial x_i} T_{ij} = -\rho\omega^2 u_j \tag{4.1}$$

$$\frac{\partial}{\partial x_i} D_i = 0 \tag{4.2}$$

$$T_{ij} = C_{ijkl} \frac{\partial u_k}{\partial x_l} + e_{ij,l} \frac{\partial \Psi}{\partial x_l} \tag{4.3}$$

$$D_i = e_{i,kl} \frac{\partial u_k}{\partial x_l} - \epsilon_{il} \frac{\partial \psi}{\partial x_l} . \tag{4.4}$$

For resonator analysis, the time harmonic assumption is employed, as in the one dimensional case, although there are numerical methods for solving time dependent wave equations as well.

The two dimension plane will be the x_1, x_2 plane with x_3 normal to it. No spatial variations are allowed along x_3. Equation (4.1) can then be rewritten,

$$\frac{\partial}{\partial x_1} T_{1j} - \frac{\partial}{\partial x_2} (-T_{2j}) = -\rho \omega^2 u_j \tag{4.5}$$

The left hand side of Eq. (4.5) can be written as a cross product by defining a vector 0 where

$$\bar{0}^{(j)} = 0_1{}^{(j)} \bar{x}_1 + 0_2{}^{(j)} \bar{x}_2 \tag{4.6}$$

and

$$0_1{}^{(j)} = -T_{2j}$$

$$0_2{}^{(j)} = T_{1j} \quad .$$

Then,

$$\nabla \times \bar{0}^{(j)} = - \rho \omega^2 u_j \quad . \tag{4.7}$$

Equation (4.7) can be written in the x_1, x_2 plane as

$$\oint_s \nabla \times \bar{0}^{(j)} \cdot d\bar{S} = - \omega^2 \int \rho u_j \cdot d\bar{S} \tag{4.8}$$

where

$$dS = dx_1 dx_2 \quad .$$

The result of having the left hand side of Eq. (4.8) in the form of a curl operation, allows a direct integration using Stoke's theorem. This reduces the expression by one order to a line integral of the stress components around a closed path in the 1, 2 plane,

$$\oint \bar{O}^{(j)} \cdot d\bar{l} = -\omega^2 \rho u_j dx_1 dx_2 \quad . \tag{4.9}$$

Physically, those integrals correspond to finding the net force on the material region.

An expression for $O_1^{(j)}$ and $O_2^{(j)}$ can be found by expanding Eq. (4.3) using the corresponding subscripts,

$$O_1^{(j)} = -T_{2j} = -C_{2jk1} \frac{\partial u_k}{\partial x_1} - C_{2jk2} \frac{\partial u_k}{\partial x_2} - e_{jk,1} \frac{\partial \Psi}{\partial x_1} - e_{2j,2} \frac{\partial \Psi}{\partial x_2}$$

and

$$O_2^{(j)} = -T_{1j} = C_{1jk1} \frac{\partial u_k}{\partial x_1} + C_{1jk2} \frac{\partial u_k}{\partial x_2} + e_{1j,1} \frac{\partial \Psi}{\partial x_1} e_{1j,2} \frac{\partial \Psi}{\partial x_2} \quad .$$

The above equations can be reduced to

$$O_1^{(j)} = -a_{jk} \frac{\partial u_k}{\partial x_1} - b_{jk} \frac{\partial u_k}{\partial x_2} \tag{4.10}$$

and

$$O_2^{(j)} = -a_{jk} \frac{\partial u_k}{\partial x_1} + d_{jk} \frac{\partial u_k}{\partial x_2} \tag{4.11}$$

by letting

$$a_{jk} = C_{2jk1} \qquad k=1,2,3$$

$$a_{jk} = e_{2j,1} \qquad k=4$$

$$b_{jk} = C_{2jk2} \qquad k=1,2,3$$

$$b_{jk} = e_{2j,2} \qquad k=4$$

$$c_{jk} = C_{1jk1} \qquad k=1,2,3$$

$$c_{jk} = e_{1j,1} \qquad k=4$$

$$d_{jk} = C_{1jk2} \qquad k=1,2,3$$

$$d_{jk} = e_{1j,2} \qquad k = 4$$

where $j = 1,2,3$

and $u_4 = \psi$.

Similarly, Eq. (4.2) can be rewritten as

$$\frac{\partial}{\partial x_1} D_1 - \frac{\partial}{\partial x_2} (-D_2) = 0 \ . \tag{4.12}$$

By defining a vector P to be

$$\bar{P} = P_1\bar{x}_1 + P_2\bar{x}_2$$

where $P_1 = -D_2$ and $P_2 = D_1$,

Equation (4.12) can be written as the cross product

$$(\nabla \times \bar{P}) = 0$$

and using Stoke's theorem as

$$\oint \bar{P} \cdot d\bar{l} = 0 \ . \tag{4.13}$$

The expressions P_1 and P_2 can be expanded with the use of Eq. (4.4),

$$P_1 = -D_2 = -e_{2,k1} \frac{\partial u_k}{\partial x_1} + \epsilon_{21} \frac{\partial \Psi}{\partial x_1} - e_{2,k2} \frac{\partial u_k}{\partial x_2} + \epsilon_{22} \frac{\partial \Psi}{\partial x_2} \tag{4.14}$$

$$P_2 = D_1 = e_{1,k1} \frac{\partial u_k}{\partial x_1} - \epsilon_{11} \frac{\partial \Psi}{\partial x_1} + e_{1,k2} \frac{\partial u_k}{\partial x_2} - \epsilon_{12} \frac{\partial \Psi}{\partial x_2} . \tag{4.15}$$

Reducing the above equations,

$$P_1 = -a_{jk} \frac{\partial u_k}{\partial x_1} - b_{jk} \frac{\partial u_k}{\partial x_2} \tag{4.16}$$

$$P_2 = c_{jk} \frac{\partial u_k}{\partial x_1} + d_{jk} \frac{\partial u_k}{\partial x_2} \tag{4.17}$$

where

$a_{jk} = e_{2,k1}$ k=1,2,3

$a_{jk} = \epsilon_{21}$ k=4

$b_{jk} = e_{2,k2}$ k=1,2,3

$b_{jk} = \epsilon_{22}$ k=4

$c_{jk} = e_{1,k1}$ k=1,2,3

$c_{jk} = -\epsilon_{11}$ k=4

$d_{jk} = e_{1,k2}$ k=1,2,3

$d_{jk} = -\epsilon_{12}$ k=4

$j = 4$ and $u_4 = \Psi$.

The subscript arrangement of Eqs. (4.10), (4.11), (4.14), and (4.15) allows those four equations to be written as

$$Q_1^{(j)} = -a_{jk} \frac{\partial u_k}{\partial x_1} - b_{jk} \frac{\partial u_k}{\partial x_2} \tag{4.18}$$

$$Q_2^{(j)} = c_{jk} \frac{\partial u_k}{\partial x_1} + d_{jk} \frac{\partial u_k}{\partial x_2} \tag{4.19}$$

where $j=1,2,3,4$ and $k=1,2,3,4$,

and the total vector Q is

$$\bar{Q}^{(j)} = Q_1^{(j)}\bar{x}_1 + Q_2^{(j)}\bar{x}_2 ,$$

which represents the sum of Eqs. (4.10), (4.11), (4.14), and (4.15). The material tensors a_{jk}, b_{jk}, c_{jk}, and d_{jk} are as previously defined.

Thus, there are four line integrals of the form

$$\oint \bar{Q} \cdot d\bar{l} = \int Q_2 dx_2 + \int Q_1 dx_1 , \tag{4.20}$$

composed of 16 terms in each of 4 regions for a total of 256 integrals, and three area integrals from Eq. (4.9) since the right hand side of Eq. (4.13) is zero.

To evaluate the line integral given by Eq. (4.20) consider the geometry shown in Fig. 4.1. The right hand side of the equation can be written as

$$\oint \bar{Q} \cdot d\bar{l} = \int_a^b Q_2 dx_2 + \int_b^c Q_1 dx_1 + \int_c^d Q_1 dx_1 + \int_d^e Q_2 dx_2 + \int_e^f Q_2 dx_2$$

$$+ \int_f^g Q_1 dx_1 + \int_g^h Q_1 dx_1 + \int_h^a Q_2 dx_2 \tag{4.21}$$

where the subscripts have been dropped and the integration limits refer to the various line segments in the four material regions, denoted by ①, ②, ③, and ④, of Fig. 4.1.

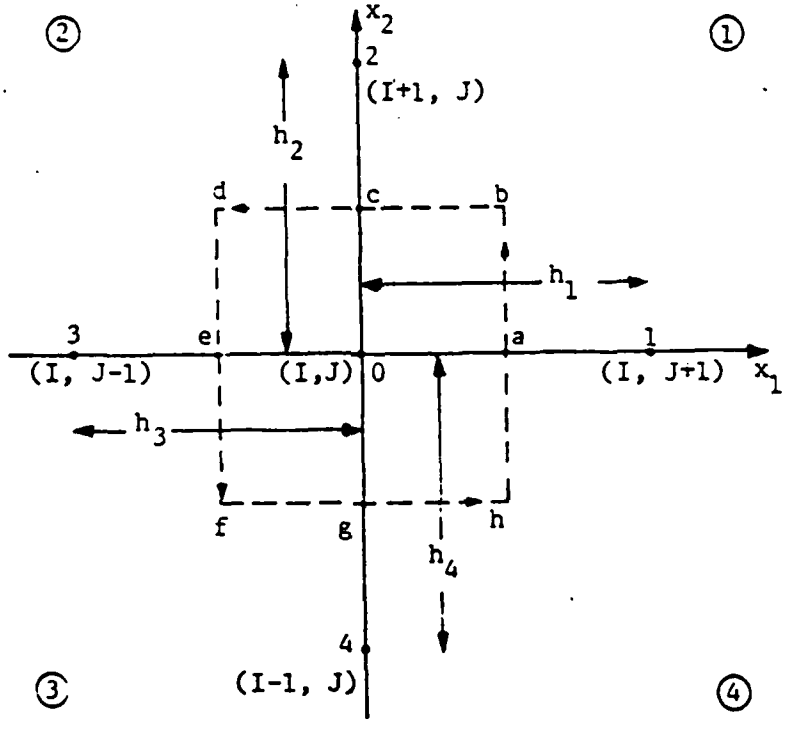

Fig. 4.1. A rectangular sampling grid in the 1,2 plane showing the method of labeling mesh points and material regions. The line integral is carried out along the a-b-c-d-e-f-g-h-a path and the area integral within the region defined by the line. The encircled numbers refer to a particular quadrant and its corresponding material constants (ρ, ϵ, C, e)

Using Eqs. (4.18) and (4.19) the right hand side of Eq. (4.21) can be evaluated and written as a function of a, b, c, and d, and the particle displacement and potential fields. For notation simplification purposes, the mesh points will be referred to as:

(I,J)	0
(I,J+1)	1
(I+1,J)	2
(I,J-1)	3
(I-1,J)	4 .

The terms involving Q_2 will be evaluated first.

$$\int_a^b Q_2 dx_2 = \int_a^b c^{(1)} \frac{\partial u}{\partial x} dx_2 + \int_a^b d^{(1)} \frac{\partial u}{\partial x} dx_2$$

$$= c^{(1)} \left(\frac{u(1) - u(0)}{h_1} \right) x_2 \Big|_0^{h_2/2} + d^{(1)} (u(b) - u(a))$$

$$= (u(1) - u(0))\, c^{(1)} \frac{h_2}{2h_1} + d^{(1)} \left(\frac{u(2) - u(0)}{2} \right) \qquad (4.22)$$

where, in general,

$$\frac{du}{dx} = \frac{u(i) - u(0)}{h_i} ,$$

i = 1-4,

and because the points are sufficiently closed together,

$$u(b) = \frac{u(2) + u(1)}{2}$$

and

$$u(a) = \frac{u(1) + u(0)}{2} .$$

In a similar way,

$$\int_h^a Q_2 dx = c^{④} \left(\frac{u(1) - u(0)}{h_1} \right) x_2 \Big|_{-h_4/2}^{0} + d^{④}(u(a) - u(h))$$

$$= (u(1) - u(0)) \frac{c^{④} h_4}{2h_1} + d^{④} \left(\frac{u(0) - u(4)}{2} \right) \qquad (4.23)$$

where

$$u(h) = \frac{u(4) + u(1)}{2} .$$

$$\int_d^e Q_2 dx_2 = c^{②} \left(\frac{u(0) - u(3)}{} \right) x_2 \Big|_{h_2/2}^{0} + d^{②}(u(e) - u(d))$$

$$= (u(0) - u(3)) \frac{c^{②} h_2}{2h_3} (-1) + d^{②} \left(\frac{u(0) - u(2)}{2} \right) \qquad (4.24)$$

where

$$u(e) = \frac{u(3) + u(0)}{2}$$

and

$$u(d) = \frac{u(3) + u(2)}{2}$$

$$\int_e^f Q_2 dx_2 = c^{(3)} \left(\frac{u(0) - u(3)}{h_3} \right) x_2 \Big|_0^{-h_4/2} + d^{(3)} (u(f) - u(e))$$

$$= (u(0) - u(3)) \frac{c^{(3)} h_4}{2h_3} (-1) + d^{(3)} \left(\frac{u(4) - u(0)}{2} \right) \quad (4.25)$$

where

$$u(f) = \left(\frac{u(3) + u(4)}{2} \right) .$$

The terms involving Q_1 can be evaluated in a similar fashion,

$$\int_b^c Q_1 dx_1 = - \int_b^c a \frac{\partial u}{\partial x_1} dx_1 - \int_b^c b \frac{\partial u}{\partial x_2} dx_1$$

$$= - a^{(i)} (u(c) - u(b)) - b^{(1)} \left(\frac{u^{(2)} - u^{(0)}}{h_2} \right) x_1 \Big|_{\substack{c=0 \\ b=h_1/2}}$$

$$= - a^{(1)} \left(\frac{u(0) - u(1)}{2} \right) - b^{(1)} (u(2) - u(0)) \left(\frac{-h_1}{2h_2} \right) \quad (4.26)$$

where

$$u(c) = \frac{u(2) + u(0)}{2}$$

and

$$u(b) = \frac{u(2) + u(1)}{2} .$$

$$\int_c^d Q_1 dx_1 = -a^{(2)} (u(d) - u(c)) - b^{(2)} \frac{(u(2) - u(0)}{h_2}) x_1 \Big|_0^{-h_3/2}$$

$$= -a^{(2)}\left(\frac{u(3) - u(0)}{2}\right) - b^{(3)}(u(2) - u(0))\left(\frac{-h_3}{2h_2}\right) \qquad (4.27)$$

where

$$u(g) = \frac{u(4) + u(0)}{2} .$$

$$\int_f^g Q_1 dx_1 = -a^{(3)}(u(g) - u(f)) - b^{(3)}\left(\frac{u(0) - u(4)}{h_4}\right) x_1 \Big|_{-h_3/2}^{0}$$

$$= -a^{(3)}\left(\frac{u(0) - u(3)}{2}\right) - b^{(3)}(u(0) - u(4))\frac{h_3}{2h_4} . \qquad (4.28)$$

And finally,

$$\int_g^h Q_1 dx_1 = -a^{(4)}(u(h) - u(g)) - b^{(4)}\left(\frac{u(0) - u(4)}{h_4}\right) x_1 \Big|_{0}^{h_1/2}$$

$$= -a^{(4)}\left(\frac{u(1) - u(0)}{2}\right) - b^{(4)}(u(0) - u(4))\frac{h_1}{2h_4} . \qquad (4.29)$$

The total line integral can be found by adding Eqs. (4.22) through (4.29). The sum can be simplified to

$$\oint \bar{Q} \cdot d\bar{l} = (u(1) - u(0))\,\alpha_1 + (u(2) - u(0))\alpha_2$$

$$+ (u(3) - u(0))\,\alpha_3 + (u(4) - u(0))\,\alpha_4 . \qquad (4.30)$$

where

$$\alpha_1 = \left[\left(\frac{c^{(1)}h_2 + c^{(4)}h_4}{2h_1}\right) + \left(\frac{a^{(1)} - a^{(4)}}{2}\right)\right] ,$$

$$\alpha_2 = \left[\left(\frac{b^{(1)}h_1 + b^{(2)}h_3}{2h_2}\right) + \left(\frac{d^{(1)} - d^{(2)}}{2}\right)\right] ,$$

$$\alpha_3 = \left[\frac{c^{(3)}h_4 + c^{(2)}h_2}{2h_3} + \left(\frac{a^{(3)} - a^{(2)}}{2}\right)\right] ,$$

and

$$\alpha_4 = \left[\left(\frac{b^{(3)}h_3 + b^{(4)}h_1}{2h_4}\right) + \left(\frac{d^{(3)} - d^{(4)}}{2}\right)\right] ,$$

where the subscript in α refers to a particular mesh point.

Consider now the area integral suggested by the right hand side of Eq. (4.9),

$$-\omega^2 \int \rho u(0) dx_1 dx_2 = -\omega^2 u(0) \int \rho dx_1 dx_2 .$$

The evaluation of the are integral yields

$$-\omega^2 u(0) \int \rho dx_1 dx_2 = -Q_0 u(0) \qquad (4.31)$$

where

$$Q_0 = \omega^2 \tilde{\rho} ,$$

where

$$\tilde{\rho} = \frac{1}{4}\left[\rho^{(1)}h_1h_2 + \rho^{(2)}h_2h_3 + \rho^{(3)}h_3h_4 + \rho^{(4)}h_4h_1\right]$$

is the effective mass per unit depth.

Since Eqs. (4.30) and (4.31) are an expanded form of the left and right hand side of Eqs. (4.9) and (4.13), they can be set equal to each other. After the subscripts are restored, the expression becomes

$$(u_k(1) - u_k(0))\alpha_{1jk} + (u_k(2) - u_k(0))\alpha_{2jk} + (u_k(3) - u_k(0))\alpha_{3jk}$$

$$+ (u_k(4) - u_k(0))\alpha_{4jk} = Q_0 u_j(0).$$

where

$k,j = 1,2,3,4$

$Q_0 = 0$ for $j = 4$,

the repeated subscript indicate a sum, and the first subscript in α refers to a particular mesh point.

The above expression can be rewritten as

$$u_k(0)\alpha_{jk} - Q_0 u_j(0) = U_j \tag{4.32}$$

where

$$U_j = u_k(1)\alpha_{1jk} + u_k(2)\alpha_{2jk} + u_k(3)\alpha_{3jk} + u_k(4)\alpha_{4jk},$$

$$\alpha_{jk} = \alpha_{1jk} + \alpha_{2jk} + \alpha_{3jk} + \alpha_{4jk},$$

and

$$\alpha_{1jk} = \frac{c^{(1)}_{jk} h_2 + c^{(4)}_{jk} h_4}{2h_1} + \frac{a^{(1)}_{jk} - a^{(4)}_{jk}}{2}$$

$$\alpha_{2jk} = \frac{b^{(1)}_{jk} h_1 + b^{(2)}_{jk} h_3}{2h_2} + \frac{d^{(1)}_{jk} - d^{(2)}_{jk}}{2}$$

$$\alpha_{3jk} = \frac{c^{(3)}_{jk} h_4 + c^{(2)}_{jk} h_2}{2h_3} + \frac{a^{(3)}_{jk} - a^{(2)}_{jk}}{2}$$

$$\alpha_{4jk} = \frac{b^{③}_{jk} h_3 + b^{④}_{jk} h_1}{2h_4} + \frac{d^{③}_{jk} - d^{④}_{jk}}{2}$$

Equation (4.32) holds at each point in the mesh and can be written as a matrix as follows,

$$\left[\begin{array}{ccc:c} \alpha_{11}-Q_o & \alpha_{12} & \alpha_{13} & \alpha_{14} \\ \alpha_{21} & \alpha_{22}-Q_o & \alpha_{23} & \alpha_{24} \\ \alpha_{31} & \alpha_{32} & \alpha_{33}-Q_o & \alpha_{34} \\ \hdashline \alpha_{41} & \alpha_{42} & \alpha_{43} & \alpha_{44} \end{array}\right] \left[\begin{array}{c} u_1(0) \\ u_2(0) \\ u_3(0) \\ u_4(0) \end{array}\right] = \left[\begin{array}{c} U_1 \\ U_2 \\ U_3 \\ U_4 \end{array}\right] \qquad (4.33)$$

where $u(0)_{1-3}$ stand for the particle displacement fields corresponding to the central mesh point along the direction given by the subscripts, and u_4 refers to the electric potential corresponding to that same central mesh point. Physically, the fields at a given mesh point are viewed as being driven by the nearest neighbors. The dashed lines in the matrix separate those parts coupled by piezoelectricity.

The material tensors a,b,c,d, can be written in matrix form as follows,

a_{jk}	k=1	2	3	4
j=1	C_{16}	C_{66}	C_{56}	e_{16}
2	C_{12}	C_{26}	C_{25}	e_{12}
3	C_{14}	C_{46}	C_{45}	e^{14}
4	e_{12}	e_{26}	e_{25}	$-\epsilon_{21}$

, (4.34)

b_{jk}	k=1	2	3	4
j=1	C_{66}	C_{26}	C_{46}	e_{26}
2	C_{26}	C_{22}	C_{24}	e_{22}
3	C_{46}	C_{24}	C_{44}	e_{24}
4	e_{26}	e_{22}	e_{24}	$-\epsilon_{22}$

, (4.35)

c_{jk}	k=1	2	3	4
j=1	C_{11}	C_{16}	C_{15}	e_{11}
2	C_{16}	C_{66}	C_{56}	e_{16}
3	C_{15}	C_{56}	C_{55}	e_{15}
4	e_{11}	e_{16}	e_{15}	$-\epsilon_{11}$

, (4.36)

d_{jk}	k=1	2	3	4
j=1	C_{16}	C_{12}	C_{14}	e_{12}
2	C_{66}	C_{26}	C_{46}	e_{26}
3	C_{56}	C_{25}	C_{45}	e_{25}
4	e_{16}	e_{12}	e_{14}	$-\epsilon_{12}$

, (4.37)

Each tensor is given in terms of the usual reduced subscript material tensors and are partitioned by the dotted lines to identify those regions associated with Laplace's equation only, the wave equation without piezoelectric coupling, and finally the piezoelectric coupling coefficients [3].

With the proper simplifications the two dimensional method can be

used to do one dimensional analysis.

4.3 Application of the 2D Method

The two dimension numerical method will be applied to a structure consisting of an electrode, a piezoelectric thin film layer, and a semiconductor substrate (see Fig. 4.2). The mass and the thickness of the electrode are going to be considered negligible in this test of the formulation. The energy trapping effect will then be solely due to the finite dimensions of the structure. A standing wave pattern due to the material discontinuities along the two dimensions under consideration will be created within the acoustic cavity when an electric potential field is applied to it.

The particle displacement field perpendicular to the 1,2 plane will be considered uncoupled from the electric potential field by assumption. This implies that the (3,4) and (4,3) positions in the tensor of Eqs. (4.34)-(4.37) will be set to zero. Three fields will be considered in the piezoelectric region: a potential field and two particle displacement fields, one along each dimension. In the substrate region, only the two particle displacement fields will be considered since the potential field decouples because of the material properties of the substrates used.

For simplicity, the electric fields fringing out the resonator structure will not be included in this work. It was considered that with an 8:1 dielectric ratio in favor of the piezoelectric material, the electric fields escaping to the outside of the cavity region could be neglected. To achieve the nonfringing effect of the stress field, the material constant ρ, c, e will be set to zero. This forces the

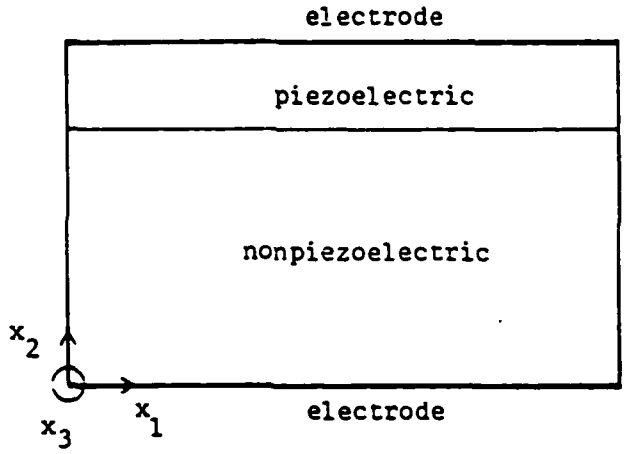

Fig. 4.2. Resonator structure and coordinate axis orientation

continuous across the boundary. Fringing could be accounted for by considering a mesh larger than the acoustic cavity structure. For continuity reasons also, the electric potential field and the force must be equal along the '2' direction across the nonpiezoelectric-piezoelectric boundary. The value of the electric potential at the electrodes, a known independent variable, becomes a part of Eq. (4.33) (see Fig. 4.3).

The resonator structure of interest requires that the piezoelectric crystal C-axis be oriented along the '2' direction. The material tensor matrices for the piezoelectric material will then have to be transformed to match the coordinate axis in use. The transformation, see Fig. 4.4, is simpler to realize when the material tensor elements are written using the abbreviated subscript notation.

As previously mentioned, the resonator structure will be divided by a mesh of vertical and horizontal lines. The value of the electric potential and particle displacement field for each mesh point will be found by using a modified version of Eq. (4.33). The third column and row of the system in Eq. (4.33) will be deleted since the particle displacement field along the '3' direction is considered uncoupled as mentioned. When expanded through the mesh structure, the set of difference equations can be written in the form of a sparse banded matrix similar to the one obtained for the one dimensional case.

For programming purposes, the frequency dependent expression Q_o will be normalized to the fundamental parallel frequency f_o of the thickness longitudinal mode in an all Si structure. The expression for Q_o was

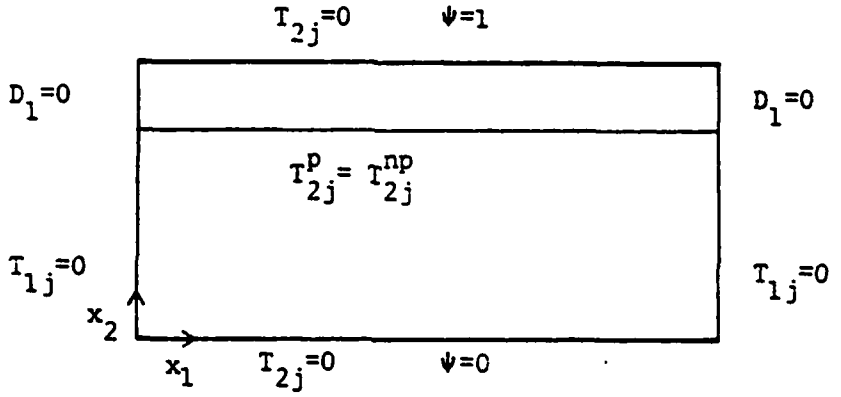

Fig. 4.3. Sample resonator structure boundary conditions where p refers to the piezoelectric region and np to the nonpiezoelectric region

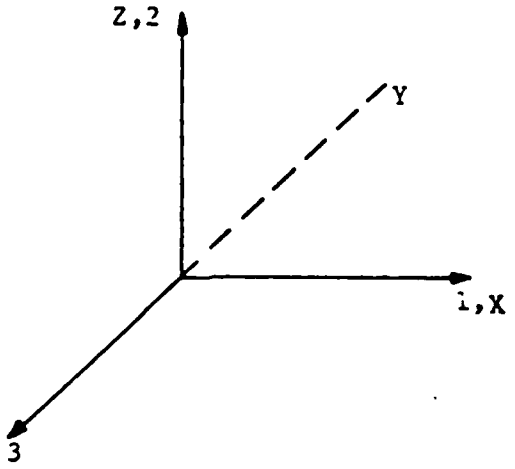

Fig. 4.4. Piezoelectric crystal axis rotation, where the X, Y, and Z refer to crystal orientation nomenclature

defined in Eq. (4.31) as

$$Q_o = \omega^2 \bar{\rho} \ . \qquad (4.38)$$

The normalization starts by defining a phase $k_o d$ as

$$k_0 d = \pi$$

from where

$$\omega_0 = \frac{\pi}{d}\sqrt{\frac{C_{11}^{Si}}{\rho^{Si}}} \qquad (4.39)$$

where C_{11}^{Si}, ρ^{Si} refer to the stiffness coefficient and mass density in Si. The normalized form of Q_0 is obtained after multiplying and dividing Eq. (4.38) by the square of Eq. (4.39),

$$Q_0 = \frac{\pi^2}{d^2}\frac{C_{11}^{Si}}{\rho^{Si}}\left(\frac{f}{f_0}\right)^2 \bar{\rho} \qquad (4.40)$$

The normalized frequency value of the above expression is dependent on the horizontal to vertical mesh point spacing ratio. When this ratio is changed, the structure's effective thickness is changed, which in turn modifies the frequency value by a square root of the spacing ratio factor.

The particle displacement and potential fields of a ZnO/Si composite structure will be modeled by a computer program. Since no comparisons with analytical results can be made for this particular structure, the

numerical results will be qualitatively evaluated.

As was noted in chapter III, a certain minimum number of mesh points is needed to determine the field waves with accuracy. Extremely large matrices can be generated if the same resolution is desired for the two dimensional case. For this reason, the modeling will be limited to frequencies close to fundamental where the fields can still be resolved using a small number of mesh points.

The particle displacement at a particular mesh point will be represented by a dot. For clarity purposes, only the waves along the perimeter of the deformed structure will be shown with solid lines. The undeformed mesh and device geometries are included as reference. The electric potential field will only be shown in the piezoelectric region since it is zero in the rest of the structure.

The particle displacement magnitudes shown in Figs. 4.5-4.7, are by no means proportional to the dimensions of the structure. Even though the latter are normalized, they are generally in the micron unit range whereas the particle displacements are in the Angstrom unit range.

Physical considerations suggest that, due to the structure of the crystals used, the particle displacement field along the '1' direction and the magnitude of the electric potential field be symmetric with respect to a vertical axis along the middle of the acoustic cavity. It is expected that, because of the Poisson's ratio[1], the particle

---

[1] It refers to the ratio of the transverse contraction per unit dimension of a bar to its elongation per unit length, when subjected to a tensile stress.

displacement along the '1' direction be larger in the ZnO. If the particle displacement and potential field results are correct, $\nabla \cdot D = 0$. Also, u and Ψ should be continuous across the ZnO/Si interface.

The expected field symmetry can be seen in Figs. 4.5-4.7. The narrow structure of Fig. 4.5a) clearly shows the effect of the Poisson terms as the structure deforms along a direction different than that of the driving electric potential. It can also be seen from this figure that the particle displacement along the '1' direction is larger in the ZnO region. The structure however, is not wide enough to sustain a standing wave resonance. Such a wave pattern can be observed in Figs. 4.6a) and 4.7a) as the horizontal to vertical dimensions ratio of the structures gets larger. Inversely proportional to this ratio is the effect of the Poisson terms. The electric potential is also symmetric as shown in Figs. 4.5b)-4.7b). The electric potential variations along the x_1 direction are directly related to the magnitude changes in the particle displacement field. These variations however, are small and impossible to resolve in the figures.

A remark about the behavior of the particle displacement field in the Fig. 4.5 structure: the larger particle displacements in the piezoelectric region are not only due to the Poisson ratio but also to an acoustic impedance mismatch. It happens that a large part of the wave generated in the piezoelectric region is reflected at the ZnO/Si boundary. The mismatch decreases as the structure becomes wider as can be seen from the behavior of the field in Figs. 4.6 and 4.7.

The no free charge condition was tested by applying the equation $\nabla \cdot \bar{D} = 0$ to a mesh point in the piezoelectric region. As expected, the

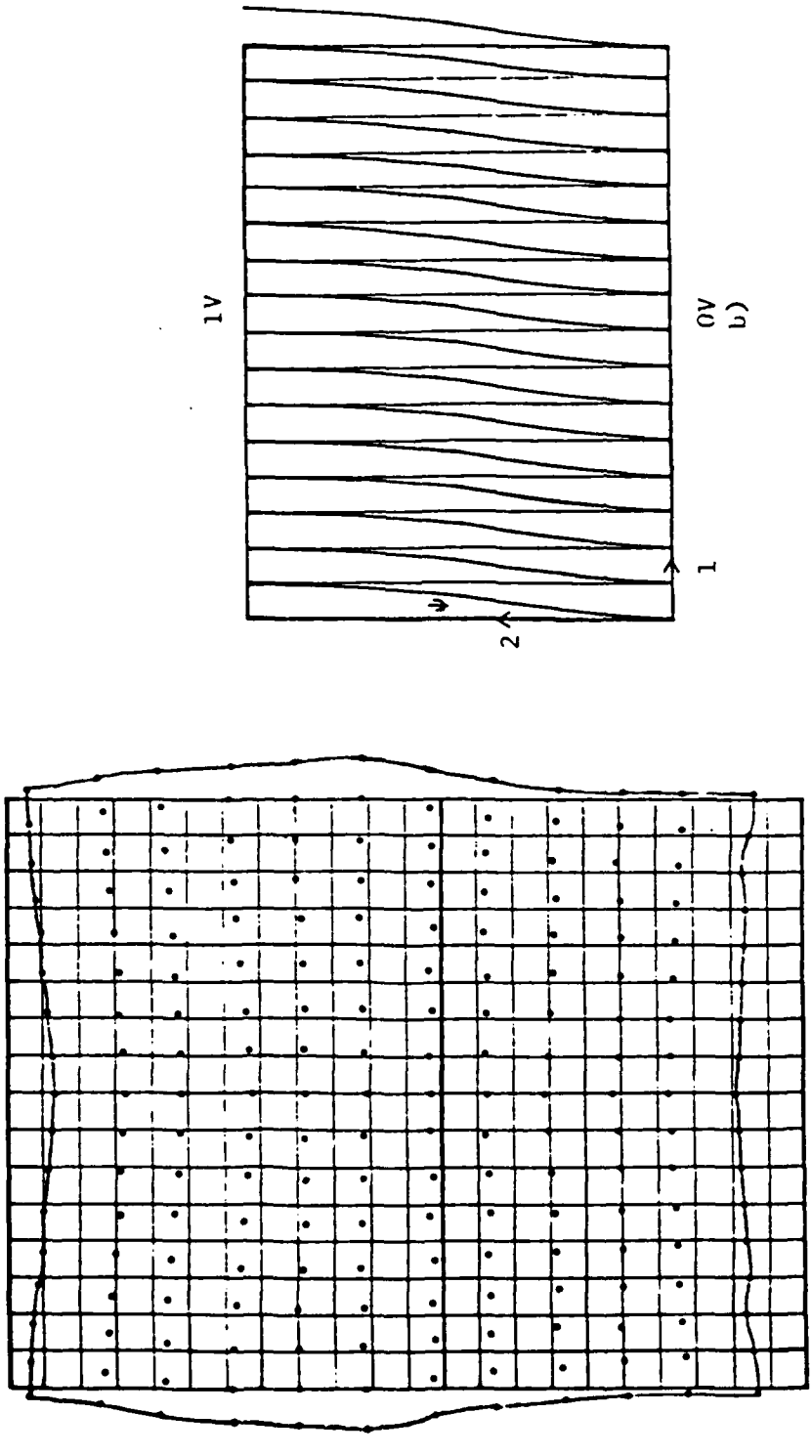

Fig. 4.5. Field configuration in a 12 vertical by 17 horizontal mesh point structure at an effective frequency of 0.636. The horizontal to vertical spacing ratio is 0.5. a) particle displacement field (0.5 cm = 1 Å displacement), b) electric potential field (volts), where the vertical lines represent 0 V reference lines

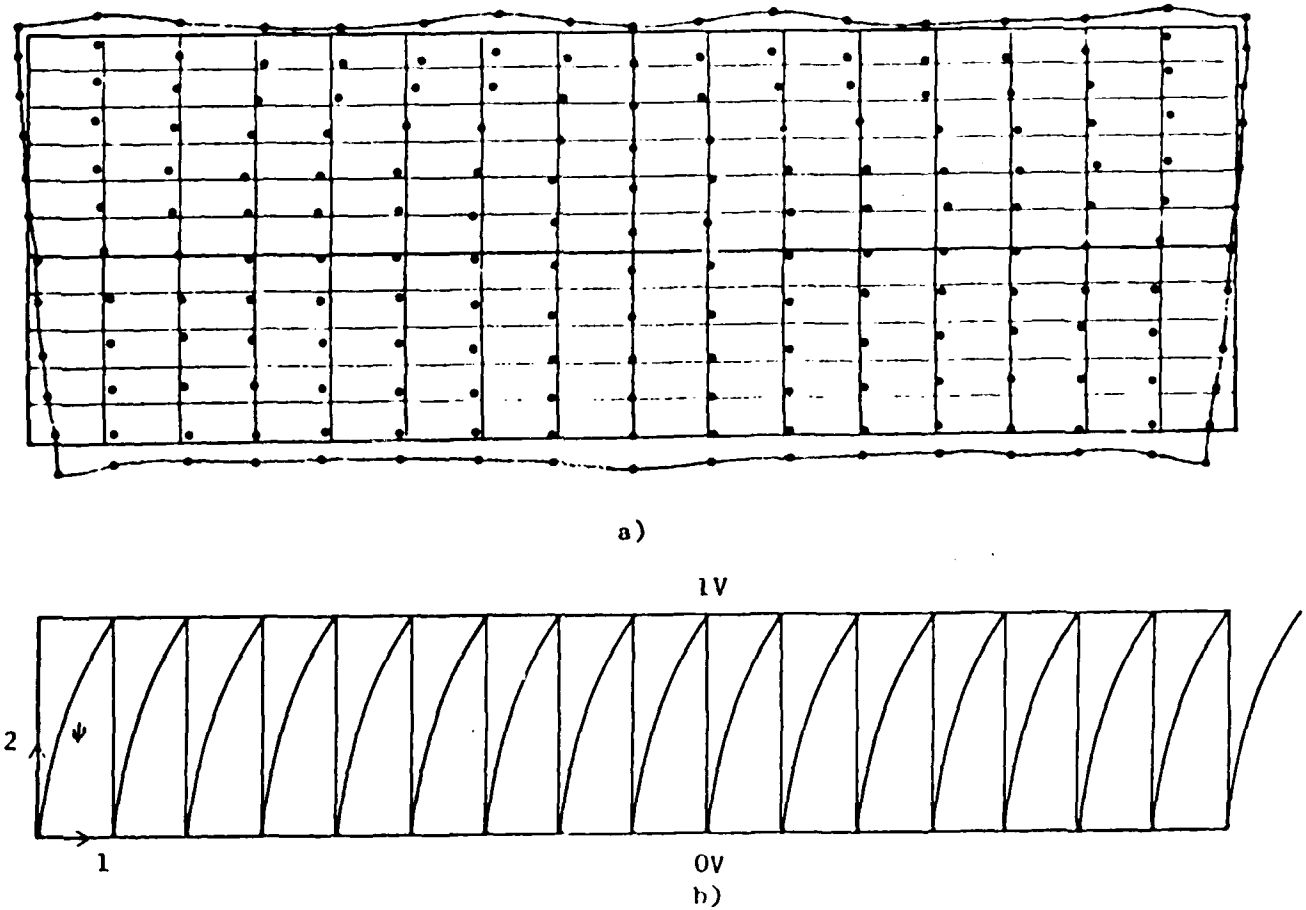

Fig. 4.6. Field configuration in a 12 vertical by 17 horizontal mesh point structure at an effective normalized frequency of 1.27. The horizontal to vertical spacing ratio is 2 a) particle displacement field (1 cm = 1 Å displacement, b) electric potential field (volts), where the vertical lines represent 0 V reference lines

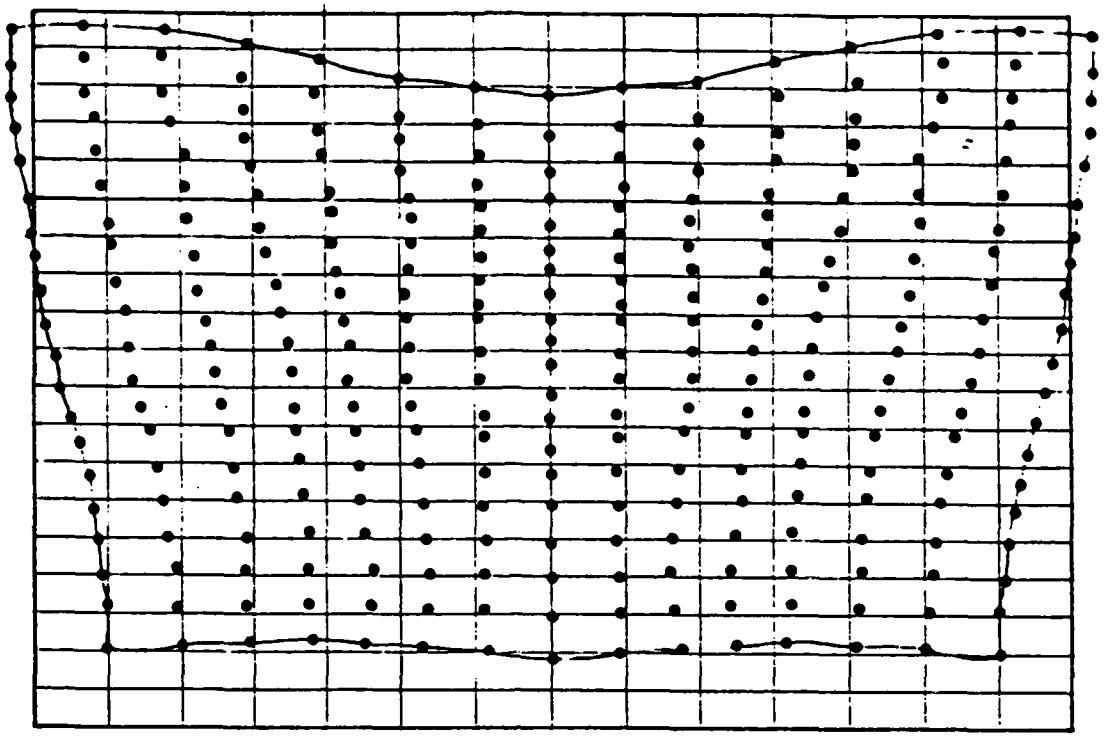

a)

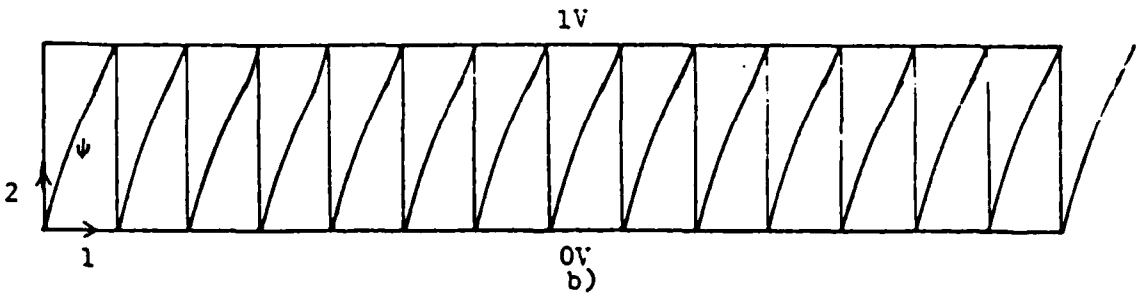

b)

Fig. 4.7. Field configuration in a 20 vertical by 15 horizontal mesh point structure at an effective normalized frequency of 1.27. The horizontal to vertical spacing ratio is 2. a) displacement field (1 cm = 1 Å displacement), electric potential field (volts)

condition holds. The continuity of the particle displacement field across the boundary can be visually confirmed by looking at the figures. The waves along both directions seem to be continuous across the material interface. A qualitative confirmation of particle displacement continuity is affected by the number of mesh points required. The continuity of the electric potential field across the discontinuity is obvious. The electric potential is zero at the interface, in this analysis, and so is the electric potential in the nonpiezoelectric region.

An impedance expression can be found by considering the electrical properties of the structure at the terminals. As for the one dimensional case, consider the expression

$$Z = \frac{V}{i\omega Da} \tag{4.41}$$

For the two dimensional case, the electric displacement D at the electrode can be approximated by

$$\int D \cdot da = a \sum_{n=1}^{L-1} D_2(n)$$

where a is the electrode area and L is the number of mesh points along the '1' direction. The electric displacement D_2, along the '2' direction, is given by

$$\sum_{n=1}^{L-1} D_2 = \sum_{n=1}^{L-1} \left(e_{13} \frac{\partial u_1}{\partial x_1} + e_{35} \frac{\partial u_1}{\partial x_2} + e_{35} \frac{\partial u_2}{\partial x_1} + e_{33} \frac{\partial u_2}{\partial x_2} - \epsilon_{31} \frac{\partial u_4}{\partial x_1} - \epsilon_{33} \frac{\partial u_4}{\partial x_2} \right) \tag{4.42}$$

where the material tensor transformation has already been performed. The above equation reduces to

$$\sum_{n=1}^{L-1} D_2 = \sum_{n=1}^{L-1} \left(e_{33} \frac{\partial u_2}{\partial x_2} - \epsilon_{33} \frac{\partial u_4}{\partial x_2} \right). \tag{4.43}$$

The impedance expression can be found by substituting Eq. (4.43) into Eq. (4.41),

$$Z = \frac{-V}{j\omega C_g \, d_2 \left(\sum_{n=1}^{L-1} \left(\frac{e_{33}}{\epsilon_{33}} \frac{\partial u_2}{\partial x_2} - \frac{\partial u_4}{\partial x_2} \right) \right)} \tag{4.44}$$

where

$$C_g = \frac{\epsilon a}{d_2} ,$$

$$j = -i ,$$

a is the area of the electrode in the x_1, x_3 plants, and d_2 is the thickness of the piezoelectric region where the capacitance effect is concentrated.

For computational purposes the impedance will be normalized to $j\omega C_g$. Figure 4.8 shows a plot of the magnitude and phase of the impedance at frequencies around fundamental series and parallel resonances. Only one resonance spectrum can be observed since just one mode is trapped in the structure of 12 vertical and 5 horizontal mesh points, a structure similar to the one shown in Fig. 4.5. Computational considerations were again a factor in choosing those particular dimensions.

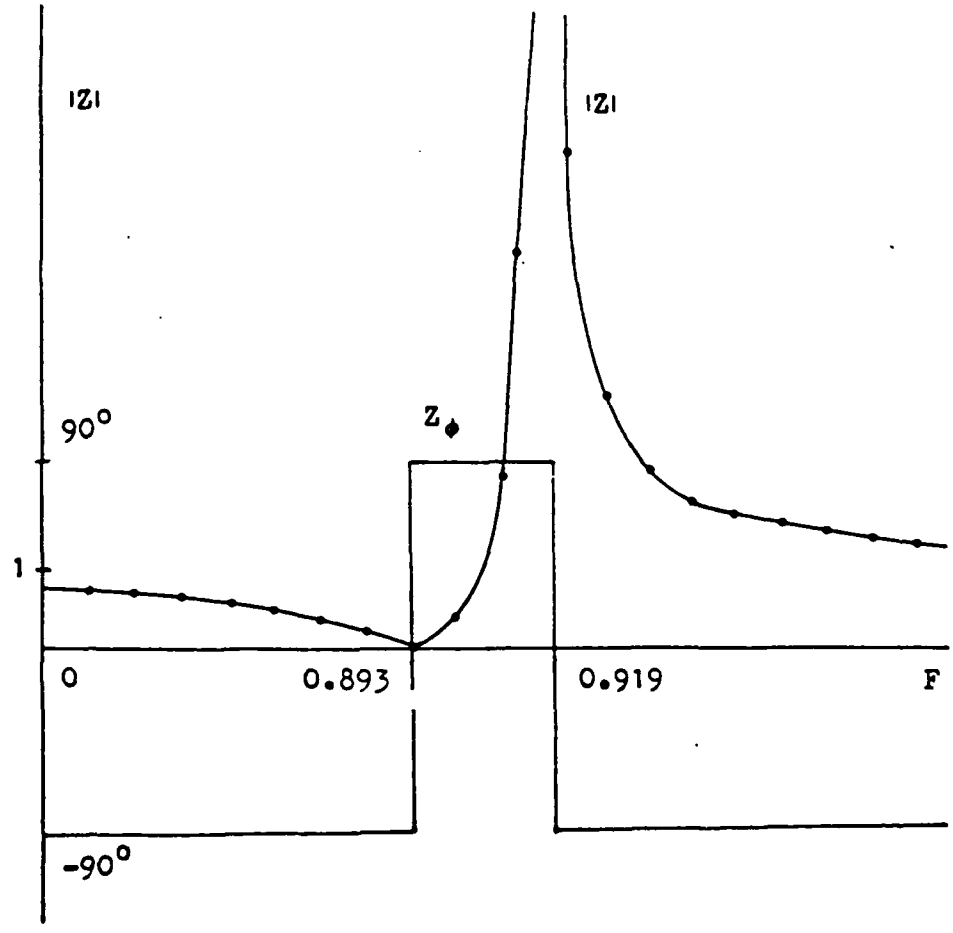

Fig. 4.8. Magnitude and phase impedance plot of a 12 vertical by 5 horizontal mesh points structure at frequencies around fundamental series and parallel resonance. The materials intersect at the sixth vertical mesh point from the bottom

At frequencies below resonance, the normalized impedance tends to 1 as in the one dimensional case. Note that the fundamental parallel resonance will not occur at a normalized frequency of 1, because of the previous normalization of the frequency to a parallel resonance frequency of an all Si acoustic cavity. The overtones though, will still occur at approximate integer multiplies of the fundamental. The series resonance will vary as given by Eq. 3.24.

The numerical impedance results and Eq. 3.24 can be used to calculate an effective coupling coefficient K^2,

$$K^2 = \frac{\phi_s}{\tan \phi_s} ,$$

from where $K^2 = 0.062$. This value can be compared to one calculated from the elastic, dielectric and piezoelectric coefficients of ZnO,

$$K^2 = \frac{m^2}{1+m^2}$$

where $m^2 = \frac{e_{33}^2}{C_{33}^E \epsilon_{33}^S}$, for a longitudinal wave,

and $m^2 = \frac{e_{15}^2}{C_{55}^E \epsilon_{11}^S}$, for a shear wave.

The effective coupling calculated from the impedance is 35% smaller than the analytic coupling calculated for a longitudinal wave, and 8% larger than the analytic coupling calculated for a shear wave. And therefore it

is concluded that the effective coupling coefficient calculated from the impedance is a combination of the coupling coefficients calculated from the two waves.

4.4 Conclusion

A two dimensional difference formulation of the general anisotropic piezoelectric coupled wave equations has been implemented for the modeling of the bulk acoustic wave resonator's wave structure. The difference equations form a coupled set of four equations describing, in a straight forward manner, the particle displacement and potential fields at each element in the mesh. The form of the equations indicate that a central mesh point is driven by its nearest neighbors. When expanded, the difference equations can be written in the form of a sparse banded matrix whose solution is obtainable by well-known techniques.

A one dimensional comparison of analytical and numerical solutions indicates that the finite difference method can be applied with excellent results.

The two dimensional numerical results satisfy the requirements of no free charge and symmetry with respect to a vertical line across the middle of the structure. The continuity of the particle displacement and potential field across the ZnO/Si interface is visually confirmed. A quantitative check was not carried out because the number of mesh points required to do so. A standing wave resonance along the x_1 direction is observed when the horizontal dimension is larger than half a wavelength. A series and parallel resonance confirm that the structure can resonate. A comparison with analytical results obtained by others, was not possible because of the difference in analyzed structures.

The two and one dimensional analysis results suggest that the

numerical method can be successfully used in modeling the two dimensional pattern inside a bulk acoustic wave composite resonator.

REFERENCES

1. Auld, B. A. Acoustic Fields and Waves in Solids. Vol. I-Vol. II. New York: John Wiley & Sons, Inc., 1973.

2. Johnson, L. W., and Reiss, R. D. Numerical Analysis. 2nd edition. Reading, Massachusets: Addison-Wesley Publishing Company, Inc., 1980.

3. Lakin, K. M. "Analysis of Composite Resonator Geometries." Proceedings of the 37th Annual Symposium on Frequency Control (1983) : 320-324.

4. Lakin, K. M. EE 590H Class Notes. Department of Electrical Engineering, Iowa State University, 1984.

5. Lakin, K. M., Wang, J. S., Kline, G. R., Landin, A. R., Chen, Y. Y., and Hunt, J. D. "Thin Film Resonators and Filters." 1982 Ultrasonics Symposium Proceedings (1982): 466-475.

6. Milsom, R. F. "Two-Dimensional Theory of Thin-Film ZnO Resonators on Silicon." 1982 Ultrasonics Symposium Proceedings (1982): 484-489.

7. Peach, R. C. "The Design of Partially Controlled Quartz Crystal Resonators." Proceedings of the 36th Annual Frequency Control Symposium (1982): 22-28.

8. Ramo, S., Whinnery, J. R., and Van Duzer, T. Fields and Waves in Communication Electronics. New York: John Wiley & Sons, Inc., 1965.

9. Sheahan, D. F., and Johnson, R. A. "Crystal and Mechanical Filters." IEEE Transactions on Circuits and Systems CAS-22 (1975): 68-69.

10. Shockley, W., Curran, D. R., and Koneval, D. J. "Trapped-Energy Modes in Quartz Filter Crystals." The Journal of the Acoustical Society of America 41, No. 4, Part 2 (1967): 224-256.

11. Smith, G. D. Numerical Solution of Partial Differential Equations. New York: Oxford University Press, 1965.

12. Tiersten, H. F., and Stevens, D. S. "An analysis of Thickness-Extensional Trapped Energy Resonators with Rectangular Electrodes in the Zinc-Oxide Thin Film on Silicon Configuration." IEEE Proceedings CH1957 (1983): 325-333.

END

11-86

DTIC